Entropy production in *pp* and Pb-Pb collisions at energies available at the CERN Large Hadron Collider

Patrick Hanus and Klaus Reygers
Physikalisches Institut, Universität Heidelberg, Im Neuenheimer Feld 226, D-69120 Heidelberg, Germany

Aleksas Mazeliauskas
Theoretical Physics Department, CERN, CH-1211 Genève 23, Switzerland
and Institut für Theoretische Physik, Universität Heidelberg, Philosophenweg 16, D-69120 Heidelberg, Germany

(Received 30 August 2019; published 4 December 2019)

We use experimentally measured identified particle spectra and Hanbury Brown-Twiss radii to determine the entropy per unit rapidity dS/dy produced in $\sqrt{s} = 7\,\text{TeV}$ *pp* and $\sqrt{s_{\text{NN}}} = 2.76\,\text{TeV}$ Pb-Pb collisions. We find that $dS/dy = 11\,335 \pm 1188$ in 0%–10% Pb-Pb, $dS/dy = 135.7 \pm 17.9$ in high-multiplicity *pp*, and $dS/dy = 37.8 \pm 3.7$ in minimum bias *pp* collisions and compare the corresponding entropy per charged particle $(dS/dy)/(dN_{\text{ch}}/dy)$ to predictions of statistical models. Finally, we use the quantum chromodynamics kinetic theory pre-equilibrium and viscous hydrodynamics to model entropy production in the collision and reconstruct the average temperature profile at $\tau_0 \approx 1\,\text{fm}/c$ for high-multiplicity *pp* and Pb-Pb collisions.

DOI: 10.1103/PhysRevC.100.064903

I. INTRODUCTION

Ultrarelativistic collisions of nuclei as studied at the Relativistic Heavy Ion Collider (RHIC) and the Large Hadron Collider (LHC) are typically modeled assuming rapid thermalization within a time scale of 1–2 fm $/c$ [1]. The subsequent longitudinal and transverse expansion of the created quark-gluon plasma (QGP) is then described by viscous relativistic hydrodynamics [2]. In this picture the bulk of the entropy is created during the thermalization process and the later stages of the evolution add relatively little [3]. By correctly accounting for the entropy production in different stages of the collisions, one can therefore relate the measurable final-state particle multiplicities to the properties of system, e.g., initial temperature, at the earlier stages of the collisions.

Two different methods are frequently used to estimate the total produced entropy in nuclear collisions. In the first method, pioneered by Pal and Pratt, one calculates the entropy based on transverse momentum spectra of different particle species and their source radii as determined from Hanbury Brown-Twiss correlations [4]. The original paper analyzed data from $\sqrt{s_{\text{NN}}} = 130\,\text{GeV}$ Au-Au collisions and is still the basis of many entropy estimations at other energies [3]. The second method uses the entropy per hadron as calculated in a hadron resonance gas model to translate the final-state multiplicity dN/dy per unit of rapidity to an entropy dS/dy [5,6]. Even though the estimate of the entropy from the measured multiplicity $dN_{\text{ch}}/d\eta$ is relatively straightforward one finds quite different values for the conversion factor between the measured charged-particle multiplicity $dN_{\text{ch}}/d\eta$ and the entropy dS/dy in the literature [6–9].

This paper provides an up-to-date calculation of entropy production in *pp* and Pb-Pb collisions at the LHC energies and uses state-of-the-art modeling of the QGP to reconstruct the initial conditions at the earliest moments in the collision. In Sec. II we recap the method of Ref. [4], which we use in Sec. III A and Sec. III B to calculate the total produced entropy per rapidity, and the entropy per final-state charged hadron $S/N_{\text{ch}} \equiv (dS/dy)/(dN_{\text{ch}}/dy)$ from the identified particle spectra and femtoscopy data for $\sqrt{s} = 7\,\text{TeV}$ *pp* and $\sqrt{s_{\text{NN}}} = 2.76\,\text{TeV}$ Pb-Pb collisions at LHC [10–16]. In Sec. IV the result for the entropy per particle is then compared to different estimates of the entropy per hadron calculated in hadron resonance gas models at the chemical freeze-out temperature of $T_{\text{ch}} \approx 156\,\text{MeV}$ [17]. Finally in Sec. V A we use different models of the QGP evolution to track entropy production in different stages of the collisions and to determine the initial temperature profile at $\tau = 1\,\text{fm}/c$.

II. ENTROPY FROM TRANSVERSE MOMENTUM SPECTRA AND HBT RADII

In this section we recap the entropy calculation from phase-space densities obtained from particle spectra and femtoscopy [4]. Foundations for this method were laid in Refs. [18,19]. The entropy S for a given hadron species at the time of kinetic freeze-out is calculated from the phase space density $f(\vec{p}, \vec{r})$

---

according to

$$S = (2J+1)\int \frac{d^3r d^3p}{(2\pi)^3}[-f\ln f \pm (1\pm f)\ln(1\pm f)], \tag{1}$$

where + is for bosons and the − for fermions. The factor $2J+1$ is the spin degeneracy. The total entropy in the collision is then given by the sum of the entropies of the produced hadrons species. The integral in Eq. (1) can be evaluated using the series expansion,

$$\pm(1\pm f)\ln(1\pm f) = f \pm \frac{f^2}{2} - \frac{f^3}{6} \pm \frac{f^4}{12} + \dots . \tag{2}$$

Three-dimensional source radii measured through Hanbury Brown-Twiss two-particle correlations [20] are usually determined in the longitudinally co-moving system (LCMS) in which the component of the pair momentum along the beam direction vanishes. The density profile of the source in the LCMS is parametrized by a three-dimensional Gaussian so that the phase space density can be written as

$$f(\vec{p},\vec{r}) = \mathcal{F}(\vec{p})\exp\left(-\frac{x_{\mathrm{out}}^2}{2R_{\mathrm{out}}^2} - \frac{x_{\mathrm{side}}^2}{2R_{\mathrm{side}}^2} - \frac{x_{\mathrm{long}}^2}{2R_{\mathrm{long}}^2}\right), \tag{3}$$

with

$$\mathcal{F}(\vec{p}) = \frac{(2\pi)^{3/2}}{2J+1}\frac{d^3N}{d^3p}\frac{1}{R_{\mathrm{out}}R_{\mathrm{side}}R_{\mathrm{long}}}. \tag{4}$$

The radii in Eqs. (3) and (4) are functions of the momentum $\vec{p}$.

In many cases only the one-dimensional source radius R_{inv}, which is determined in the pair rest frame (PRF), can be determined experimentally owing to limited statistics. In Ref. [4] the relation between R_{inv} in the PRF and the three-dimensional radii in the LCMS was assumed to be

$$R_{\mathrm{inv}}^3 \approx \gamma R_{\mathrm{out}}R_{\mathrm{side}}R_{\mathrm{long}}, \tag{5}$$

where $\gamma = m_{\mathrm{T}}/m \equiv \sqrt{m^2+p_{\mathrm{T}}^2}/m$. This is also our standard assumption. In [21] and [22] the ALICE collaboration reported values for both R_{inv} and R_{out}, R_{side}, R_{long} obtained from two-pion correlations in Pb-Pb collisions at $\sqrt{s_{\mathrm{NN}}} = 2.76$ TeV and *pp* collisions at $\sqrt{s} = 7$ TeV, respectively. From these results one can determine a more general version of Eq. (5) of the form $R_{\mathrm{inv}}^3 \approx h(\gamma)R_{\mathrm{out}}R_{\mathrm{side}}R_{\mathrm{long}}$ with $h(\gamma) = \alpha\gamma^\beta$. Results for the entropy dS/dy obtained under this assumption are given in Appendix A.

Using Eq. (5) one arrives at

$$\frac{dS}{dy} = \int dp_T\, 2\pi p_T\, E\frac{d^3N}{d^3p}\left(\frac{5}{2} - \ln\mathcal{F} \pm \frac{\mathcal{F}}{2^{5/2}} - \frac{\mathcal{F}^2}{2\times 3^{5/2}} \pm \frac{\mathcal{F}^3}{3\times 4^{5/2}}\right), \tag{6}$$

with

$$\mathcal{F} = \frac{1}{m}\frac{(2\pi)^{3/2}}{2J+1}\frac{1}{R_{\mathrm{inv}}^3(m_{\mathrm{T}})}E\frac{d^3N}{d^3p}, \tag{7}$$

where *m* is the particle mass and + is for bosons and − for fermions. Note that Eq. (6) includes the terms up to $f_i^4/12$ of the Taylor expansion in Eq. (2).

Pions have the highest phase space density of the considered hadrons and the approximation made in Eq. (6) is better than 1% for pions in central Pb-Pb collisions at $\sqrt{s_{\mathrm{NN}}} = 2.76$ TeV. In *pp* collisions at $\sqrt{s} = 7$ TeV the maximum pion phase space density $\mathcal{F}(p_{\mathrm{T}})$ exceeds unity at low p_{T} rendering the series expansion in Eq. (2) unreliable. For pions in *pp* collisions we therefore approximate the $(1+f)\ln(1+f)$ term of Eq. (1) by a polynomial of order 8. This gives an approximate expression with numerical coefficients a_i which is also valid for values of $\mathcal{F}$ obtained for pions in high-multiplicity *pp* collisions:

$$\frac{dS}{dy} = \int dp_T\, 2\pi p_T\, E\frac{d^3N}{d^3p}\left(\frac{5}{2} - \ln\mathcal{F} + \sum_{i=0}^{7} a_i\mathcal{F}^i\right). \tag{8}$$

TABLE I. Estimate of the entropy $(dS/dy)_{y=0}$ for 0%–10% most central Pb-Pb collisions at $\sqrt{s_{\mathrm{NN}}} = 2.76$ TeV. The table shows the hadrons considered as stable final-state particles and their contribution to the total entropy.

Particle	$(dS/dy)_{y=0}^{\text{one state}}$	Factor	$(dS/dy)_{y=0}^{\text{total}}$
π	2182	3	6546
K	605	4	2420
η	399	1	399
η'	66	1	66
p	266	2	532
n	266	2	532
Λ	160	2	320
Σ	58	6	348
Ξ	39	4	156
Ω	8	2	16
Total			11 335

III. RESULTS

A. Entropy in Pb-Pb collisions at $\sqrt{s_{\mathrm{NN}}} = 2.76$ TeV

We determine the entropy in Pb-Pb collisions at $\sqrt{s_{\mathrm{NN}}} = 2.76$ TeV for the 10% most central collisions considering as final-state hadrons the particles given in Table I. The calculation uses transverse momentum spectra of π, K, p [10], Λ [11], and Ξ, Ω [12] from the ALICE collaboration as experimental input. We also use HBT radii measured by ALICE [23].

For the entropy determination the measured transverse momentum spectra need to be extrapolated to $p_{\mathrm{T}} = 0$. To this end we fit different functional forms to the p_{T} spectra (Tsallis, Bose-Einstein, exponential in transverse mass $m_{\mathrm{T}} = \sqrt{p_{\mathrm{T}}^2+m^2}$, Boltzmann, as defined in [10]). In the entropy calculation we only use the extrapolations in p_{T} regions where data are not available; otherwise we used the measured spectra. Differences of the entropy estimate for different functional form are taken as a contribution to the systematic uncertainty. We have checked that the p_{T}-integrated π, K, p multiplicities $(dn/dy)_{y=0}$ agree with the values published in [10].

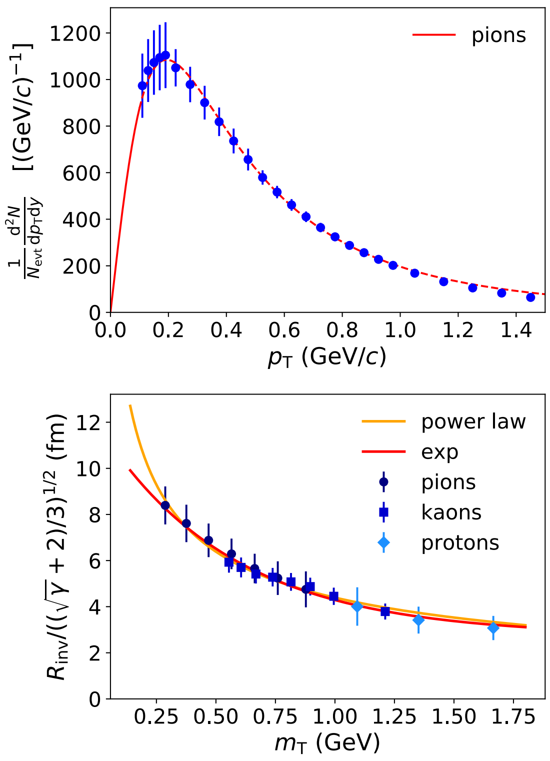

FIG. 1. Transverse momentum spectrum of positive pions (top) and scaled HBT radii R_{inv} (bottom) in 0%–10% Pb-Pb collisions at $\sqrt{s_{\mathrm{NN}}} = 2.76$ TeV. A Tsallis function [24,25] is fitted to the spectrum to extrapolate to $p_T = 0$. The one-dimensional HBT radii divided by $((\sqrt{\gamma}+2)/3)^{1/2}$ [26] where $\gamma = m_T/m$ as a function of the transverse mass m_T are parametrized by a power law function αm_T^{β} and by an exponential function $a\exp(-m_T/b) + c$.

The one-dimensional invariant HBT radii R_{inv} are only available for π, K, and p. When plotted as a function of transverse mass $m_T = \sqrt{m^2 + p_T^2}$ the R_{inv} values for these particles do not fall on a common curve. However, in [26] it was shown that the HBT radii R_{inv} divided by $((\sqrt{\gamma}+2)/3)^{1/2}$ where $\gamma = m_T/m$ are approximately a function of m_T only. This empirical scaling factor for R_{inv} is related to the fact that for a three-dimensional Gaussian parametrization of the source the one-dimensional source distribution in general cannot be described by a Gaussian (see Appendix of [26]). We use this m_T scaling of the scaled HBT radii to obtain $R_{\mathrm{inv}}(m_T)$ for all considered particles. The bottom panel of Fig. 1 shows parametrizations of the scaled HBT radii with a power law function and with an exponential function which provide different extrapolation towards the pion mass. We propagate the systematic uncertainties of the measured HBT radii as well as the uncertainty related to the two different parametrizations to the uncertainty of the extracted entropy.

For the entropy calculation the particle species in Table I are considered stable. The entropy carried by neutrons, neutral kaons, η, η', and Σ baryons is estimated based on measured species assuming that the entropy per particle is similar for particles with similar masses. The entropy carried by neutrons is assumed to be the same as the entropy carried by protons. The entropy associated with neutral kaons and η mesons is determined from charged kaons, the entropy of η' from protons, and the entropy of Σ baryons from Λ.

The yields of particles in Table I contain contributions from strong decays. To take into account mass differences and to estimate the contributions from strong decays to the different particle species we simulate particle decays with the aid of PYTHIA 8.2 [27,28]. To this end we generate primary particles available in PYTHIA 8.2 with rates proportional to equilibrium particle densities in a noninteracting hadron gas [29,30]:

$$n = \sum_{k=1}^{\infty} \frac{Tg}{2\pi^2}\frac{(\pm)^{k+1}}{k} m^2 \mathrm{K}_2\left(\frac{km}{T}\right) e^{k\mu/T}. \tag{9}$$

Here $g = 2J + 1$ is the spin degeneracy factor and K_2 the modified Bessel function of the second kind. The + is for bosons and the − for fermions. For the chemical potential we use $\mu = 0$. For the temperature we take $T = 156$ MeV as obtained from statistical model fits to particle yields measured at the LHC [17]. We then simulate strong and electromagnetic decays of the primary particles. Particle ratios after decays are used to estimate the entropy of unmeasured particles. In case of the η meson we find that after decays the η/K^+ ratio is 0.69 while the primary ratio is $\eta_{\mathrm{prim}}/\mathrm{K}^+_{\mathrm{prim}} = 0.79$. For the η' we find $\eta'_{\mathrm{prim}}/\mathrm{p}_{\mathrm{prim}} = 0.45$ and $\eta'/\mathrm{p} = 0.25$ after decays. The primary $\Sigma^-_{\mathrm{prim}}/\Lambda_{\mathrm{prim}}$ ratio is about 0.66. The entropy carried by the Σ baryons is derived from the ratios $\Sigma^-/\Lambda \approx 0.26$ and $\Sigma^0/\Lambda \approx 0.27$ after decays.

The η, η' mesons and Σ^0 baryons decay electromagnetically. Decay products from these decays ($\eta, \eta' \to$ pions, and $\Sigma^0 \to \Lambda\gamma$) are not subtracted from the experimentally determined particle spectra. As η, η', and Σ are considered stable in the entropy calculation (see Table I) we correct for this feed-down contributions. In the particle decay simulation described above we determine the feed-down fraction,

$$R_{\mathrm{fd}}(X \to Y) = \frac{\text{number of } Y \text{ from } X}{\text{total number of } Y}, \tag{10}$$

and find $R_{\mathrm{fd}}(\eta \to \pi^+) = 3.6\%$, $R_{\mathrm{fd}}(\eta' \to \pi^+) = 1.2\%$, $R_{\mathrm{fd}}(\eta' \to \eta) = 5.9\%$, and $R_{\mathrm{fd}}(\Sigma^0 \to \Lambda) = 27.0\%$.

The entropies for the particle species considered stable are summarized in Table I. These values represent the average of the entropies obtained for the power law and the exponential parametrization of the scaled invariant HBT radii. In both cases the Tsallis function was used to extrapolate the measured transverse momentum spectra to $p_T = 0$. We considered the uncertainties of the measured transverse momentum spectra, the choice of the parametrization of the p_T spectra, the uncertainties of the measured HBT radii, and the choice of the parametrization of the HBT radii as a function of m_T as sources of systematic uncertainties. The estimated total entropy in 0%–10% most central Pb-Pb collisions at $\sqrt{s_{\mathrm{NN}}} = 2.76$ TeV is $11\,335 \pm 1188$. The uncertainty of the estimated entropy is the quadratic sum of the uncertainties related to the transverse momentum spectra ($\sigma_{\mathrm{spectra}} = 629$) and invariant HBT radii ($\sigma_{R_{\mathrm{inv}}} = 1007$).

It is interesting to calculate the entropy per charged hadron in the final state from the total entropy. From [31] we obtain for 0%–10% most central Pb-Pb collisions at $\sqrt{s_{\rm NN}} = 2.76$ TeV a charged-particle multiplicity at midrapidity of $dN_{\rm ch}/d\eta = 1448 \pm 54$. From our parametrizations of the pion, kaon, and proton spectra we find a Jacobian for the change of variables from pseudorapidity to rapidity of $(dN_{\rm ch}/dy)/(dN_{\rm ch}/d\eta) = 1.162 \pm 0.008$. This yields an entropy per charged hadron in the final state of $S/N_{\rm ch} = 6.7 \pm 0.8$.

In the paper by Pratt and Pal the entropy was determined for the 11% most central Au-Au collisions at a center-of-mass energy of $\sqrt{s_{\rm NN}} = 130$ GeV. The total entropy per unit of rapidity around midrapidity was found to be $dS/dy = 4451$ with an estimated uncertainty of 10%. Using $dN_{\rm ch}/dy = 536 \pm 21$ from [32] and $(dN_{\rm ch}/dy)/(dN_{\rm ch}/d\eta) \approx 1.15$ we find an entropy per charged particle of $S/N_{\rm ch} \equiv (dS/dy)/(dN_{\rm ch}/dy) = 7.2 \pm 0.8$. This value for Au-Au collisions at a center-of-mass energy of $\sqrt{s_{\rm NN}} = 130$ GeV agrees with the value of $S/N_{\rm ch} = 6.7 \pm 0.8$ we obtain for the LHC energy in this paper.

B. Entropy in *pp* collisions at $\sqrt{s} = 7$ TeV

Not only in high-energy nucleus-nucleus collisions but also in proton-proton and proton-nucleus collisions transverse momentum spectra and azimuthal distributions of produced particles can be modeled assuming a hydrodynamic evolution of the created matter [33–35]. This provides a motivation to determine the entropy dS/dy with the Pal-Pratt method also in *pp* collisions. Moreover, the experimentally determination of the entropy is of interest in the context of models which are based on entropy production mechanisms not related to particle scatterings (see, e.g., [36,37]). Here we focus on minimum bias and high-multiplicity *pp* collisions at $\sqrt{s} = 7$ TeV.

Transverse momentum spectra for both minimum bias collisions (π, K, p [13], Λ [11], and Ξ, Ω [14]) and high-multiplicity *pp* collisions (π, K, p [15], Λ, Ξ, Ω [16]) are taken from the ALICE experiment. The high-multiplicity sample (class I in [16] and [15]) roughly corresponds to the 0%–1% percentile of the multiplicity distribution measured at forward and backward pseudorapidities. HBT radii are taken from [22]. In minimum bias *pp* collisions there is little dependence of $R_{\rm inv}$ on transverse mass and a constant value $R_{\rm inv} = 1.1 \pm 0.1$ fm is assumed. For the high-multiplicity sample $m_{\rm T}$ scaling of $R_{\rm inv}$ is assumed and the same power law and exponential functional forms as in the Pb-Pb analysis are fit to the data from [22] ($N_{\rm ch} = 42$–51 class in [22]). Taking into account the uncertainty of associating the multiplicity class in [15,16] with the one in [22] we assume an uncertainty of $R_{\rm inv}$ for the high-multiplicity sample of about 10%.

With the same assumptions for the contribution of unobserved particles and feed-down as in Pb-Pb collisions we obtain $dS/dy|_{\rm MB} = 37.8 \pm 3.7$ in minimum bias (MB) collisions and $dS/dy|_{\rm HM} = 135.7 \pm 17.9$ for the high-multiplicity (HM) sample. The contribution of the different particle species to the total entropy are given in Tables II and III. With $dN_{\rm ch}/d\eta = 6.0 \pm 0.1$ [38] and $(dN_{\rm ch}/dy)/(dN_{\rm ch}/d\eta) = 1.21 \pm 0.01$ for minimum bias *pp* collisions we obtain $S/N_{\rm ch}|_{\rm MB} = 5.2 \pm 0.5$ for the entropy per final-state charged particle. For the high-multiplicity sample with $dN_{\rm ch}/d\eta = 21.3 \pm 0.6$ [15] and $(dN_{\rm ch}/dy)/(dN_{\rm ch}/d\eta) = 1.19 \pm 0.01$ we find $S/N_{\rm ch}|_{\rm HM} = 5.4 \pm 0.7$.

TABLE II. Estimate of the entropy $(dS/dy)_{y=0}$ in minimum bias *pp* collisions at $\sqrt{s} = 7$ TeV.

Particle	$(dS/dy)_{y=0}^{\rm one\ state}$	Factor	$(dS/dy)_{y=0}^{\rm total}$
π	6.7	3	20.1
K	2.1	4	8.4
η	1.4	1	1.4
η'	0.3	1	0.3
p	1.2	2	2.4
n	1.2	2	2.4
Λ	0.6	2	1.2
Σ	0.2	6	1.2
Ξ	0.1	4	0.4
Ω	0.01	2	0.02
Total			37.8

IV. COMPARISONS TO STATISTICAL MODELS

To compare the $S/N_{\rm ch}$ value determined from the measured final-state particle spectra to calculations in which particles originate from a hadron resonance gas one needs to know the ratio $N/N_{\rm ch}$ of the total number of primary hadrons $N(\equiv N_{\rm prim})$ to the total number of measured charged hadrons in the final state $N_{\rm ch}(\equiv N_{\rm ch}^{\rm final})$. The latter contains feed-down contributions from strong and electromagnetic hadron decays. If only pions were produced one would get $N/N_{\rm ch} = 3/2$. With the aforementioned PYTHIA 8.2 simulation and the list of stable hadrons implemented in PYTHIA [again with hadron yields given by Eq. (9) for $T = 156$ MeV and $\mu_{\rm b} = 0$] we obtain a value of $(N/N_{\rm ch})_{\rm Pythia} = 1.14$. In this calculation particles with a lifetime τ above 1 mm/c were considered stable. Using the implementation of the hadron resonance gas of Ref. [39] we find $(N/N_{\rm ch})_{\rm TF} = 1.09$. In the following we use $N/N_{\rm ch} = 1.115 \pm 0.03$, i.e., we take the average of the two results as central value and the difference as a measure of the uncertainty.

TABLE III. Estimate of the entropy $(dS/dy)_{y=0}$ in high-multiplicity *pp* collisions (class I in [16] and [15])) at $\sqrt{s} = 7$ TeV.

Particle	$(dS/dy)_{y=0}^{\rm one\ state}$	Factor	$(dS/dy)_{y=0}^{\rm total}$
π	23.8	3	71.4
K	7.5	4	30.0
η	4.9	1	4.9
η'	1.0	1	1.0
p	4.2	2	8.4
n	4.2	2	8.4
Λ	2.3	2	4.6
Σ	0.8	6	4.8
Ξ	0.5	4	2.0
Ω	0.1	2	0.2
Total			135.7

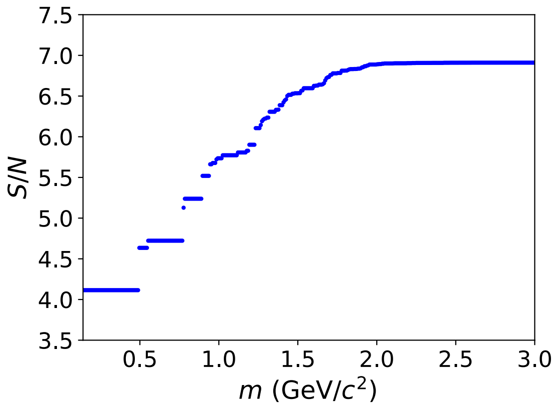

FIG. 2. Entropy per primary hadron S/N for a noninteracting thermal hadron resonance gas at a temperature of $T = 156$ MeV as given by Eq. (12) as a function of the upper mass limit for particles listed in the particle data book [40]. The entropy per hadron saturates for high upper mass limits at a value of $S/N = 6.9$.

In the simplest form of the description of a hadron resonance gas the system is treated as a noninteracting gas of pointlike hadrons where hadronic resonances have zero width. The entropy density for a primary hadron with mass m at thermal equilibrium with temperature T and vanishing chemical potential $\mu = 0$ is then given by [30]

$$s = \frac{4gT^3}{2\pi^2}\sum_{k=1}^{\infty}\frac{(\pm)^{k+1}}{k^4}\left[\left(\frac{km}{T}\right)^2 \mathrm{K}_2\left(\frac{km}{T}\right) + \frac{1}{4}\left(\frac{km}{T}\right)^3 \mathrm{K}_1\left(\frac{km}{T}\right)\right], \quad (11)$$

where + is for bosons and − for fermions. K_1 and K_2 are modified Bessel functions of the second kind. Using Eqs. (9) and (11) the entropy per primary hadron in the thermal hadron resonance gas can be calculated as

$$S/N = \frac{\sum_i s_i}{\sum_i n_i}, \quad (12)$$

where the index i denotes the different particles species. For illustration, the entropy per hadron is shown in Fig. 2 as a function of the upper limit on the mass for all particles listed in the particle data book [40].

More sophisticated implementations of the hadron resonance gas take the volume of the hadrons and the finite width of hadronic resonances into account [17,39,41–48]. Some of these models implement chemical nonequilibrium factors which we do not consider here. Models can also differ in the set of considered hadron states. In the following we concentrate on the models by Braun-Munzinger *et al.* [17] ("model 1") and Vovchenko and Stöcker [39] ("model 2"). The corresponding values for the entropy per primary hadron S/N and the entropy per final-state charged hadron S/N_{ch} are given in Table IV. The S/N_{ch} values for these models are somewhat larger than the measured value of $S/N_{\mathrm{ch}} = 6.7 \pm 0.8$, but the deviations are not larger than 1–2σ. We note here that the two approaches calculate slightly different quantities. Our estimate is based on the nonequilibrium distributions of a few final state hadrons, while Eq. (12) sums the entropy contributions of all primary hadrons in a thermal state before the decays. Although on general grounds we expect the total entropy to increase during the decays and rescatterings in the hadronic phase, there are some decay products, e.g., photons, which are not included in our current entropy count. Accounting for such differences between the two approaches might bring the estimates closer together.

TABLE IV. Entropy per primary hadron S/N at a temperature of $T = 156$ MeV for different hadron resonance gas models. The entropy per final-state charged hadron is calculated from S/N by multiplying with the factor $N/N_{\mathrm{ch}} = 1.115 \pm 0.03$. The volume correction of model 2 is based on the quantum van der Waals model. Within 1–2σ the S/N_{ch} values of these models agree with the value of $S/N_{\mathrm{ch}} = 6.7 \pm 0.8$ obtained from data.

Model	S/N	S/N_{ch}
Simple HRG [Eq. (12)]	6.9	7.7 ± 0.2
Model 1 (Braun-Munzinger *et al.* [17,49])		
Without volume correction	7.3	8.1 ± 0.2
With volume correction	7.6	8.5 ± 0.2
Model 2 (Vovchenko, Stöcker [39])		
Ideal	6.9	7.7 ± 0.2
With volume correction, zero width	7.2	8.1 ± 0.2
With volume correction, finite width	7.1	7.9 ± 0.2

V. INITIAL CONDITIONS AND ENTROPY PRODUCTION

A. Pb-Pb collisions

The entropy in nuclear collisions, which we calculated in previous sections, is not created instantaneously, but rather the entropy production takes place in several stages in nuclear collisions [3]. In this section we will use different models to describe the boost invariant expansion and, in particular, to determine the average initial conditions in 0%–10% most central Pb-Pb collisions at $\sqrt{s_{\mathrm{NN}}} = 2.76$ TeV at time $\tau_0 = 1$ fm.

First, we can make an estimate of the initial temperature $T(\tau_0)$ by simplifying the early time evolution of the QGP. As it was done in the original work by Bjorken [50], we will consider a one-dimensional boost-invariant expansion of homogeneous plasma with the transverse extent determined by the geometry of the nuclei, i.e., the transverse area A. The time evolution of the energy density is then solely a function of proper time τ and the assumed constituent equation for the longitudinal pressure $P_L = \tau^2 T^{\eta\eta}$. For collisionless gas with $P_L = 0$, the energy density falls as $e \propto \tau^{-1}$, i.e., energy per rapidity $dE/dy = e\tau A$ is constant [50]. For an ideal fluid with equation of state $p = c_s^2 e$, where c_s is the (constant) speed of sound, the energy density decreases faster, $e \propto \tau^{-1-c_s^2}$, because of the work done against the longitudinal pressure [50–52]. However, total entropy per rapidity $dS/dy = s\tau A$ stays constant irrespective of the equation of state as long as viscous dissipation can be neglected [50–53]. Below we compare the initial temperature estimates at time $\tau_0 = 1$ fm obtained from the final entropy dS/dy and energy dE/dy using, respectively, isentropic ideal fluid and free-streaming evolutions of QGP[1].

Assuming that the subsequent near ideal hydrodynamic evolution does not change the total entropy per rapidity dS/dy (which is also true for free-streaming expansion) the initial entropy density is equal to

$$s(\tau_0) = \frac{1}{A\tau_0} \frac{dS}{dy}\bigg|_{y=0}. \tag{13}$$

Using for the transverse area $A = \pi R_{\mathrm{Pb}}^2$ with $R_{\mathrm{Pb}} = 6.62\,\mathrm{fm}$ [55,56] gives an initial entropy density for the 0%–10% most central Pb-Pb collisions at $\sqrt{s_{\mathrm{NN}}} = 2.76\,\mathrm{TeV}$,

$$s(\tau_0) = 82.3\,\mathrm{fm}^{-3}. \tag{14}$$

According to the lattice QCD equation of state [57,58], this corresponds to a temperature,

$$T(\tau_0) \approx 340\,\mathrm{MeV}. \tag{15}$$

The transverse energy at midrapidity for the 10% most Pb-Pb collisions at $\sqrt{s_{\mathrm{NN}}} = 2.76\,\mathrm{TeV}$ was measured to be $dE_{\mathrm{T}}/dy \approx 1910\,\mathrm{GeV}$ [59,60]. Using again $A = \pi R_{\mathrm{Pb}}^2$ with $R_{\mathrm{Pb}} = 6.62\,\mathrm{fm}$ as an approximation for the transverse overlap area the initial energy density can be calculated according to the Bjorken formula [50],

$$e(\tau_0) = \frac{1}{A\tau_0} \frac{dE_{\mathrm{T}}}{dy}\bigg|_{y=0}, \tag{16}$$

which gives an energy density $e(\tau_0) \approx 13.9\,\mathrm{GeV/fm}^3$. This would correspond to much lower initial temperature $T(\tau_0) \approx 305\,\mathrm{MeV}$. This is because Eq. (16) is derived under the assumption of a constant energy per rapidity [50]. This holds for a free-streaming (or pressureless) expansion, but in hydrodynamics the system cools down faster from work done against the longitudinal pressure. Taking $\tau_{\mathrm{f}} = R_{\mathrm{Pb}}$ as a rough estimate for the lifetime of the fireball, ideal hydrodynamics predicts an $(\tau_{\mathrm{f}}/\tau_0)^{\frac{1}{3}} \approx 1.9$ times larger initial energy density, which would revise the initial temperature estimate upwards to $T(\tau_0) \approx 355\,\mathrm{MeV}$ and closer to the value we obtained from the entropy method.

Instead of assuming a constant entropy density in a collision, it is more realistic to use an entropy density profile $s(\tau, \vec{r})$, where $\vec{r}$ is a two-dimensional vector in the transverse plane (we still assume boost invariance in the longitudinal direction). We will employ the two-component optical Glauber model to construct the transverse profile of initial entropy density [61]. In this model the initial entropy is proportional to the participant nucleon number and the number of binary collisions. For a collision at impact parameter $\vec{b}$, the entropy profile is then

$$s(\tau_i, \vec{r}; \vec{b}) = \frac{\kappa_s}{\tau_i}\left(\frac{1-\alpha}{2}\frac{dN^{\mathrm{part}}(\vec{r}, \vec{b})}{d^2r} + \alpha\frac{dN^{\mathrm{coll}}(\vec{r}, \vec{b})}{d^2r}\right), \tag{17}$$

where $\kappa_s(1-\alpha)/2$ is entropy per rapidity per participant and $\kappa_s\alpha$ is entropy per rapidity per binary collision. The number densities are calculated using the nucleon-nucleon thickness functions (see Appendix B for details), and the value $\alpha = 0.128$ reproduces centrality dependence of multiplicity [56]. We average over the impact parameter $|\vec{b}| \leqslant 4.94\,\mathrm{fm}$ to produce entropy profile corresponding to 0%–10% centrality bin of Pb-Pb collisions at $\sqrt{s_{\mathrm{NN}}} = 2.76\,\mathrm{TeV}$ [56]. The overall normalization factor κ_s is adjusted to reproduce the final-state entropy estimated in Sec. III A, which depends on the expansion model. To simulate the evolution and entropy production in nucleus-nucleus collisions we employ two recently developed models: kinetic pre-equilibrium propagator KøMPøST [62,63], and viscous relativistic hydrodynamics code FLUIDUM [64].[2] For simplicity we employ a constant value of specific shear viscosity η/s and vanishing bulk viscosity ζ/s throughout the evolution.

KøMPøST uses linear response functions obtained from QCD kinetic theory[3] to propagate and equilibrate the highly anisotropic initial energy momentum tensor, which can be specified at an early starting time $\tau_{\mathrm{EKT}} = 0.1\,\mathrm{fm}$. We specify the initial energy-momentum tensor profile to be[4]

$$T^{\mu\nu}(\tau_{\mathrm{EKT}}, \vec{r}) = e(\tau_{\mathrm{EKT}}, \vec{r})\,\mathrm{diag}\left(1, \tfrac{1}{2}, \tfrac{1}{2}, 0\right). \tag{18}$$

At the end of KøMPøST evolution all components of the energy momentum tensor, the energy density, transverse flow, and the shear-stress components, are passed to the hydrodynamic model at fixed time $\tau_{\mathrm{hydro}} = 0.6\,\mathrm{fm}$.

The FLUIDUM package solves the linearized Israel-Stewart-type hydrodynamic equations around an azimuthally symmetric background profile. In this work we propagate the radial background profile until the freeze-out condition is met, which we define by a constant freeze-out temperature $T_{\mathrm{fo}} = 156\,\mathrm{MeV}$. Above this temperature the equation of state is that of lattice QCD [58]. Unless otherwise stated, we use a constant specific shear viscosity $\eta/s = 0.08$ and vanishing bulk viscosity $\zeta/s = 0$.

We start by showing the temperature evolution in the hydrodynamic phase in Fig. 3. The combined solid and dotted white lines represent the freeze-out line at $T_{\mathrm{fo}} = 156\,\mathrm{MeV}$. The dashed horizontal line indicates the spatial slice of the fireball at some fixed time τ and above the freeze-out temperature. We now can define entropy as an integral of the entropy current su^μ over a hypersurface Σ_i where Σ_i is one or more of the contours shown in Fig. 3. We define the total entropy in

---

[1] For initial energy estimates at even earlier times, see a recent publication [54], where a generalized constitutive equation of a hydrodynamic attractor was considered.

[2] We neglect the entropy production in the hadronic phase and match the entropy on the freeze-out surface.

[3] The current implementation of KøMPøST uses results of pure glue simulations, but recent calculations with full QCD degrees of freedom indicate that the evolution of the total energy-momentum tensor will not be significantly altered by chemical equilibration [65,66].

[4] As a purely practical tool we use a lattice equation of state to convert entropy density profile obtained from the Glauber model Eq. (17) to the energy density needed to initialize KøMPøST, even though the system at $\tau_{\mathrm{EKT}} = 0.1\,\mathrm{fm}$ is not in thermodynamic equilibrium.

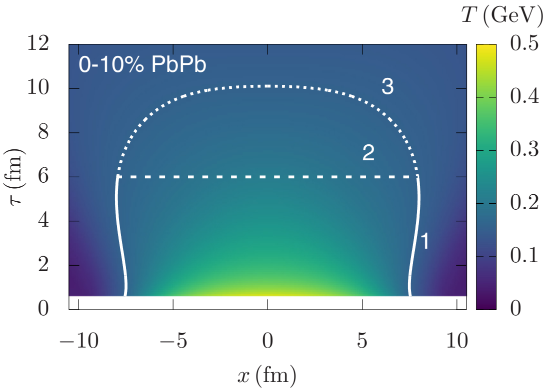

FIG. 3. Temperature in hydrodynamic evolution of an averaged 0%–10% Pb-Pb event at $\sqrt{s_{\rm NN}} = 2.76\,\text{TeV}$. Lines 1 and 3 are the freeze-out $T_{\rm fo} = 156\,\text{MeV}$ contour, whereas line 2 indicates a constant time contour in the QGP phase, i.e., $T(\tau, \vec{r}) > T_{\rm fo}$. Initial conditions for hydrodynamics at $\tau_{\rm hydro} = 0.6\,\text{fm}$ were provided by KøMPøST pre-equilibrium evolution from the starting time of $\tau_{\rm EKT} = 0.1\,\text{fm}$.

the QGP state at time τ as the integral over the contour 2:

$$S(\tau)|_{\rm QGP} \equiv \int_{\Sigma_2(\tau)} d\sigma_\mu s u^\mu. \tag{19}$$

To include the entropy outflow from the QGP because of freeze-out we also define entropy on the contours $\Sigma_1(\tau' < \tau) + \Sigma_2(\tau)$:

$$S(\tau)|_{\rm QGP+freeze\text{-}out} \equiv \int_{\Sigma_1(\tau'<\tau)+\Sigma_2(\tau)} d\sigma_\mu s u^\mu. \tag{20}$$

Because of viscous dissipation $S(\tau)|_{\rm QGP+freeze\text{-}out}$ increases until the temperature in every hydrocell drops below the freeze-out temperature and the maximum value is simply the entropy current integral over the freeze-out surface $\Sigma_1(\tau' < \tau) + \Sigma_3(\tau' > \tau)$. In Fig. 4(a) we show the time dependence of entropy per rapidity in the QGP phase (yellow line) and including freeze-out outflow (green line) in hydrodynamically expanding plasma. The solid lines are for the simulation with $\eta/s = 0.08$ and dashed lines correspond to $\eta/s = 0.16$. In both cases the initial entropy profile, Eq. (17), is adjusted so that after the pre-equilibrium (KøMPøST) and hydrodynamic (FLUIDUM) evolution the final entropy on the freeze-out surface is equal to $dS/dy = 11\,335$ estimated in Sec. III A. We see that at early times entropy is produced rapidly, but there is little entropy outflow through the freeze-out surface. At $\tau \approx 2\,\text{fm}$ the entropy in the hot QGP phase starts to drop because matter is crossing the freeze-out surface and at $\tau \approx 10\,\text{fm}$ there is no hot QGP phase left.

Here we note that the early time viscous entropy production in the hydrodynamic phase depends strongly on the initialization of the shear-stress tensor. In this work we use the pre-equilibrium propagator KøMPøST, which provides all components of the energy-momentum tensor at the hydrodynamic starting time and the shear-stress tensor approximately satisfies the Navier-Strokes constitutive equations [62,63]. We determine that for evolution with $\eta/s = 0.08$ the entropy per rapidity at time $\tau_0 = 1.0\,\text{fm}$ is ≈95% of the final entropy on the freeze-out. For twice larger shear viscosity the entropy production doubles and to produce the same final entropy we need only ≈90% at $\tau_0 = 1.0\,\text{fm}$. Such entropy production is neglected in the naive estimate of Eq. (13).

Analogously to entropy, we use the same contours to define energy in the collision, that is, as integrals of the energy current eu^μ. In Fig. 4(b) we show the energy per rapidity in different phases of the collision. We confirm that the energy per rapidity decreases rapidly in the hydrodynamic phase and at $\tau_0 = 1.0\,\text{fm}$ is nearly twice larger than on the freeze-out surface and therefore invalidating the naive initial energy density estimates using the Bjorken formula Eq. (16). However, we do note that the magnitude of the final energy per rapidity in our event is below the measured value. In

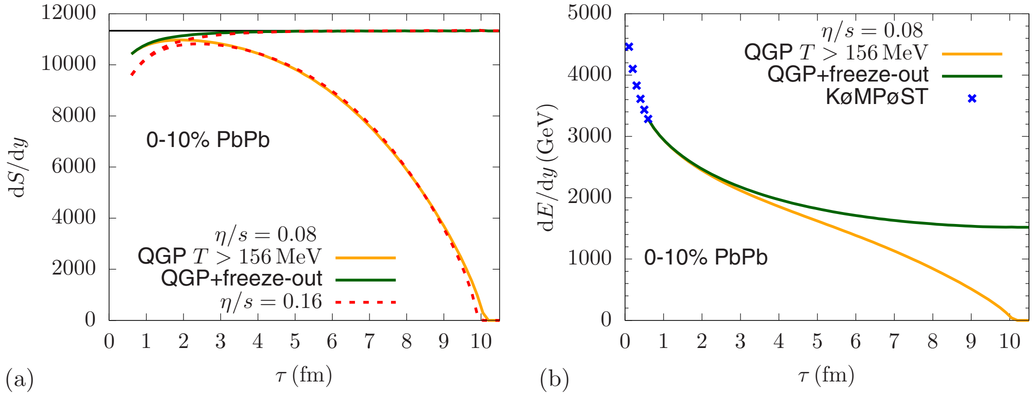

FIG. 4. (a) Entropy per rapidity in viscous hydrodynamic expansion with specific shear viscosity $\eta/s = 0.08$ for central $\sqrt{s_{\rm NN}} = 2.76\,\text{TeV}$ Pb-Pb collisions (centrality class 0%–10%) as a function of time of contour 2 in Fig. 3. The yellow line corresponds to entropy in the QGP phase ($T(\tau, r) > T_{\rm fo}$) (contour 2 in Fig. 3), whereas the green line shows the total cumulative entropy (contour 1 + 2 in Fig. 3). Dashed red lines show the corresponding result for a simulation with $\eta/s = 0.16$. In both cases the initial conditions, i.e., parameter κ_s in Eq. (17), were tuned to reproduce the final freeze-out entropy $dS/dy = 11\,335$ after the pre-equilibrium and hydrodynamic evolutions. (b) Analogous plot for energy per rapidity in hydrodynamic expansion with $\eta/s = 0.08$. The additional points show energy per rapidity in the pre-equilibrium stage.

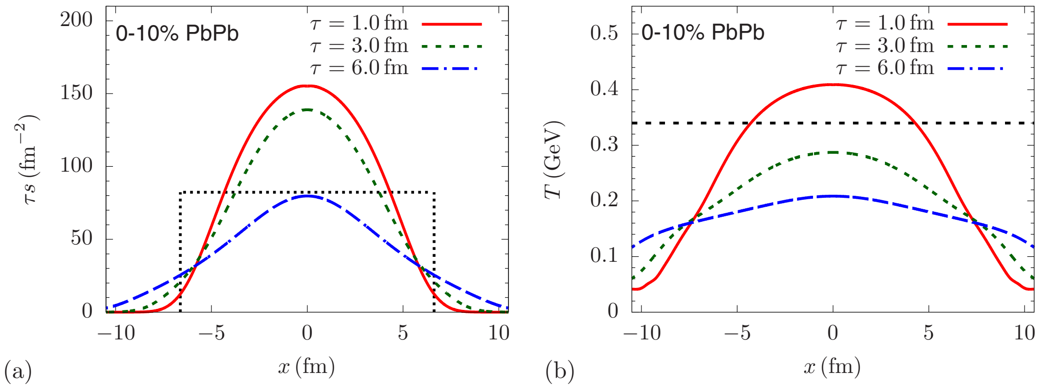

FIG. 5. (a) Entropy density profile (multiplied by τ) in viscous hydrodynamic simulation with $\eta/s = 0.08$ at times $\tau = 1, 3, 6$ fm. The black dotted square indicates the initial entropy density estimate $\tau_0 s(\tau_0) = 82.3\,\text{fm}^{-2}$; see Eq. (13). (b) Temperature profile at $\tau = 1, 3, 6$ fm. The black dotted line corresponds to $T = 340$ MeV.

addition we show points for the energy per rapidity in the pre-hydrophase simulated by KøMPøST. Despite the large anisotropy in the initial energy-momentum tensor ($T^{zz} \approx 0$ initially), the energy per rapidity is rapidly decreasing in this phase. We note that at the same time there is a significant entropy production in the kinetic pre-equilibrium evolution [63].

Next in Fig. 5(a) we look at the transverse entropy density profile $\tau s(\tau, \vec{r})$ at different times $\tau = 1.0, 3.0, 6.0$ fm in the hydrodynamic evolution with $\eta/s = 0.08$. We see that the profile changes only little between 1 fm and 3 fm, which is because of an approximate one-dimensional expansion and viscous entropy production. At later times the profile expands radially and drops in magnitude. The black-dotted line indicates the naive estimate of entropy density $\tau_0 s(\tau_0) = 82.3\,\text{fm}^{-2}$ for a disklike profile with radius $R_{\text{Pb}} = 6.62$ fm; see Eq. (14). Despite an overestimation of the net entropy at $\tau_0 = 1$ fm, the actual density at the center of entropy profile is twice larger than the naive estimate. Correspondingly, the transverse temperature profile at $\tau_0 = 1$ fm, shown in Fig. 5(b), is larger than the simple estimate and can reach 400 MeV in the center of the fireball.

B. Central *pp* collisions

In this section we present a similar analysis of entropy production in ultracentral *pp* collisions. Because of much smaller initial size, the QGP fireball (if created), has a much shorter lifetime than the central Pb-Pb collisions. This should enhance the relative role of the pre-equilibrium physics of QGP formation.

To model the initial entropy density in *pp* collision, we use a Gaussian parametrization of the transverse entropy distribution,

$$s(\tau_0, \vec{r}) = \frac{\kappa_s}{\tau_0 2\pi\sigma^2} e^{-\frac{r^2}{2\sigma^2}}, \tag{21}$$

with a width $\sigma = 0.6$ fm, as used in other parametrizations [67]. We use a fixed value of $\eta/s = 0.08$ and, in view of the range of applicability of the linearized pre-equilibrium propagator, we use KøMPøST for a shorter time from $\tau_{\text{EKT}} = 0.1$ fm to $\tau_{\text{hydro}} = 0.4$ fm.

First we show the temperature evolution in Fig. 6 and indicate the freeze-out contour (lines 1 and 3). We note that because of the compact initial size, the transverse expansion is so explosive that the center of the fireball actually freezes out before the edges (similar results were found in Refs. [68,69]). Next in Fig. 7(a) we show the entropy evolution in the QGP phase and together with the outflow from through the freeze-out surface. In a smaller system, the radial flow builds up faster and the QGP and the combined QGP+ freeze-out surface contributions starts to deviate early. This does not capture the entropy which already left $T > T_{\text{fo}}$ region in the KøMPøST phase, but for the early hydro starting time τ_{hydro}, this fraction is small. We see that as a fireball of QGP ultracentral *pp* collisions have a lifetime just above $\tau = 2$ fm. Therefore the $\tau_0 = 1$ fm reference time is no longer adequate time to discuss the "initial conditions" in such collisions. Next, in Fig. 7(b) we show the energy per rapidity in the

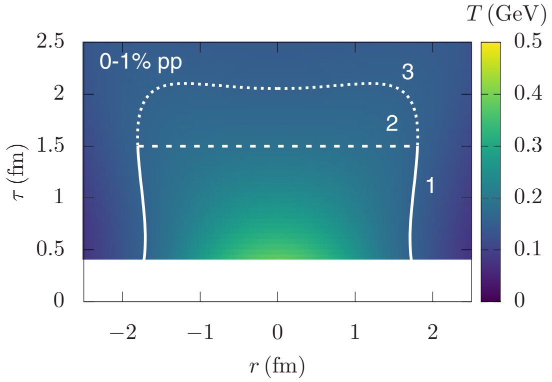

FIG. 6. Temperature in hydrodynamic evolution of an averaged 0%–1% *pp* event at $\sqrt{s} = 7$ TeV. Lines 1 and 3 are the freeze-out $T_{\text{fo}} = 156$ MeV contour, whereas line 2 indicates a constant time contour in the QGP phase, i.e., $T(\tau, \vec{r}) > T_{\text{fo}}$. Initial conditions for hydrodynamics at $\tau_{\text{hydro}} = 0.4$ fm were provided by KøMPøST pre-equilibrium evolution from the starting time of $\tau_{\text{EKT}} = 0.1$ fm.

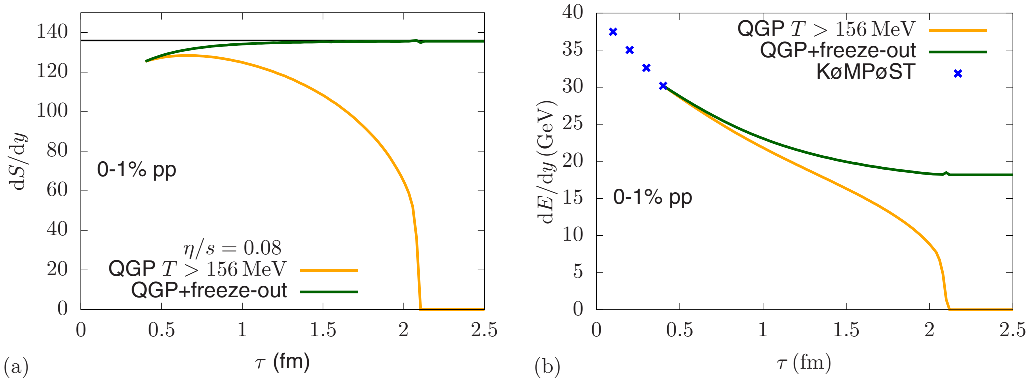

FIG. 7. (a) Entropy per rapidity in viscous hydrodynamic expansion with specific shear viscosity $\eta/s = 0.08$ for $\sqrt{s} = 7$ TeV*pp* collisions (0%–1% collisions with the highest multiplicity) as a function of time of contour 2 in Fig. 6. The yellow line corresponds to entropy in the QGP phase ($T(\tau, r) > T_{\mathrm{fo}}$) (contour 2 in Fig. 6), whereas the green line shows the total cumulative entropy (contour 1 + 2 in Fig. 6). The initial conditions, i.e., parameter κ_s in Eq. (21), was tuned to reproduce the final freeze-out entropy $dS/dy = 135.7$ after the pre-equilibrium and hydrodynamic evolutions. (b) Analogous plot for energy per rapidity in hydrodynamic expansion with $\eta/s = 0.08$. Additional points show energy per rapidity in the pre-equilibrium stage.

hydrodynamic and pre-equilibrium stages. Here again we see that energy per rapidity decreases more rapidly in comparison of entropy production.

For the transversely resolved picture of entropy and temperature profiles, we supply Figs. 8(a) and 8(b) correspondingly. At $\tau_0 = 1$ fm the maximum entropy density is much smaller than in 0%–10% centrality Pb-Pb collisions and only at $\tau = 0.5$ fm the temperature at the center reaches above $T = 300$ MeV.

VI. SUMMARY AND CONCLUSIONS

We provide independent determination of the final-state entropy dS/dy in $\sqrt{s} = 7$ TeV *pp* and $\sqrt{s_{\mathrm{NN}}} = 2.76$ TeV Pb-Pb collisions from the final phase space density calculated from the experimental data of identified particle spectra and HBT radii. In addition, we have calculated the entropy per final-state charged hadron $(dS/dy)/(dN_{\mathrm{ch}}/dy)$ in different collision systems. We find the following values for *pp* and Pb-Pb collisions.

System	dS/dy	$(dS/dy)/(dN_{\mathrm{ch}}/dy)$
Pb-Pb, 0%–10%	11 335 ± 1188	6.7 ± 0.8
pp minimum bias	37.8 ± 3.7	5.2 ± 0.5
pp high multiplicity	135.7 ± 17.9	5.4 ± 0.7

We compare our results for $(dS/dy)/(dN_{\mathrm{ch}}/dy)$ ratio based on experimental data, to the values obtained from the statistical hadron resonance gas model at the chemical freeze-out temperature of $T_{\mathrm{ch}} = 156$ MeV. For the 0%–10% most central Pb-Pb collisions statistical model values are systematically higher than our estimate, but in agreement at the 1–2σ level. However, the measured $(dS/dy)/(dN_{\mathrm{ch}}/dy)$ values in minimum bias and high-multiplicity *pp* collisions at $\sqrt{s} = 7$ TeV are below the theory predictions for a chemically equilibrated resonance gas at $T_{\mathrm{ch}} = 156$ MeV, perhaps indicating that full chemical equilibrium is not reached in these collisions. Here we note that, interestingly, in *pp* collisions the estimated soft pion phase-space density exceeds unity. Finally, we have checked the dependence of our results on the relation between

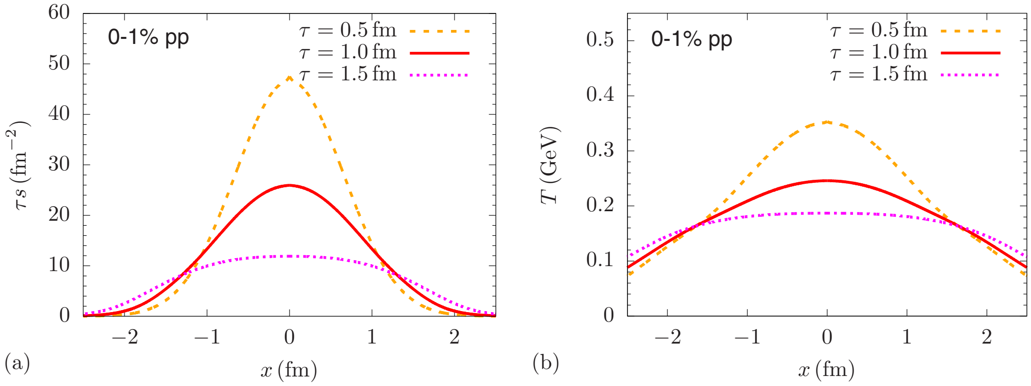

FIG. 8. (a) Entropy density profile (multiplied by τ) in viscous hydrodynamic simulation with $\eta/s = 0.08$ at times $\tau = 0.5, 1.0, 1.5$ fm. (b) Corresponding temperature profiles at $\tau = 0.5, 1.0, 1.5$ fm.

one-dimensional and three-dimensional HBT radii, Eq. (5), in Appendix A. We found no significant change for Pb-Pb results, but *pp* entropy increased by 10%, which corresponds to 1σ deviation from the results above using Eq. (5).

The precise knowledge of the total produced entropy in heavy ion collisions and the entropy per final-state charged hadron is important for constraining the bulk properties of the initial-state from the final-state observables [54,62,66]. To determine the initial medium properties for high-multiplicity *pp* and Pb-Pb collisions, we performed simulations of averaged initial conditions starting at $\tau_0 = 0.1\,\mathrm{fm}/c$ with kinetic pre-equilibrium model KøMPøST [62,63,70] and viscous relativistic hydrodynamics code FLUIDUM [64]. Importantly, these calculations take into account the produced entropy and work done in both the pre-equilibrium and hydrodynamic phases of the expansion [50–54]. We find that for simulations with the specific shear viscosity value $\eta/s = 0.08$ the initial pre-equilibrium energy per unity rapidity is about three times larger than at the final state in 0%–10% most central Pb-Pb collisions at $\sqrt{s_{\mathrm{NN}}} = 2.76\,\mathrm{TeV}$, and approximately twice larger in high-multiplicity *pp* collisions at $\sqrt{s} = 7\,\mathrm{TeV}$. At the time $\tau = 1\,\mathrm{fm}/c$, the temperature in the center of the approximately equilibrated QGP fireball is about $T \approx 400\,\mathrm{MeV}$ for Pb-Pb and $T \approx 250\,\mathrm{MeV}$ for high-multiplicity *pp* collision systems. Finally, we note that in our simulations of Pb-Pb collisions with $\eta/s = 0.08$ only about 5% of the total final entropy is produced after $\tau = 1\,\mathrm{fm}/c$, meaning that most of entropy production occurs in the pre-equilibrium phase.

ACKNOWLEDGMENTS

The authors thank Stefan Floerchinger, Eduardo Grossi, and Jorrit Lion for sharing the FLUIDUM package and useful discussions. A.M. thanks Giuliano Giacalone, Oscar Garcia-Montero, Sören Schlichting, and Derek Teaney for helpful discussions. Moreover, P.H. and K.R. thank Dariusz Miskowiec and Johanna Stachel for valuable discussions. This work is apart of and supported by the Deutsche Forschungsgemeinschaft (DFG) Collaborative Research Centre "SFB 1225 (ISOQUANT)."

APPENDIX A: RELATION BETWEEN THE 1D HBT RADIUS R_{inv} AND THE 3D HBT RADII R_{out}, R_{side}, R_{long}

A transformation of the three-dimensional Gaussian HBT radii from the longitudinally co-moving system (LCMS) to the pair rest frame (PRF) only affects the outwards direction according to $R_{\mathrm{out}}^{\mathrm{PRF}} = \gamma R_{\mathrm{out}}^{\mathrm{LCMS}}$ where $\gamma = m_{\mathrm{T}}/m \equiv \sqrt{m^2 + p_{\mathrm{T}}^2}/m$. For a three-dimensional Gaussian parametrization of the source, the one-dimensional distribution in radial distance from the origin is not in general a one-dimensional Gaussian. Therefore, there is no exact formula relating the radius R_{inv} of the one-dimensional Gaussian parametrization of the source and R_{out}, R_{side}, R_{long} [26].

The maximum phase space density $\mathcal{F}$ for a more general version of Eq. (5) of the form,

$$R_{\mathrm{inv}}^3 \approx h(\gamma) R_{\mathrm{out}} R_{\mathrm{side}} R_{\mathrm{long}}, \tag{A1}$$

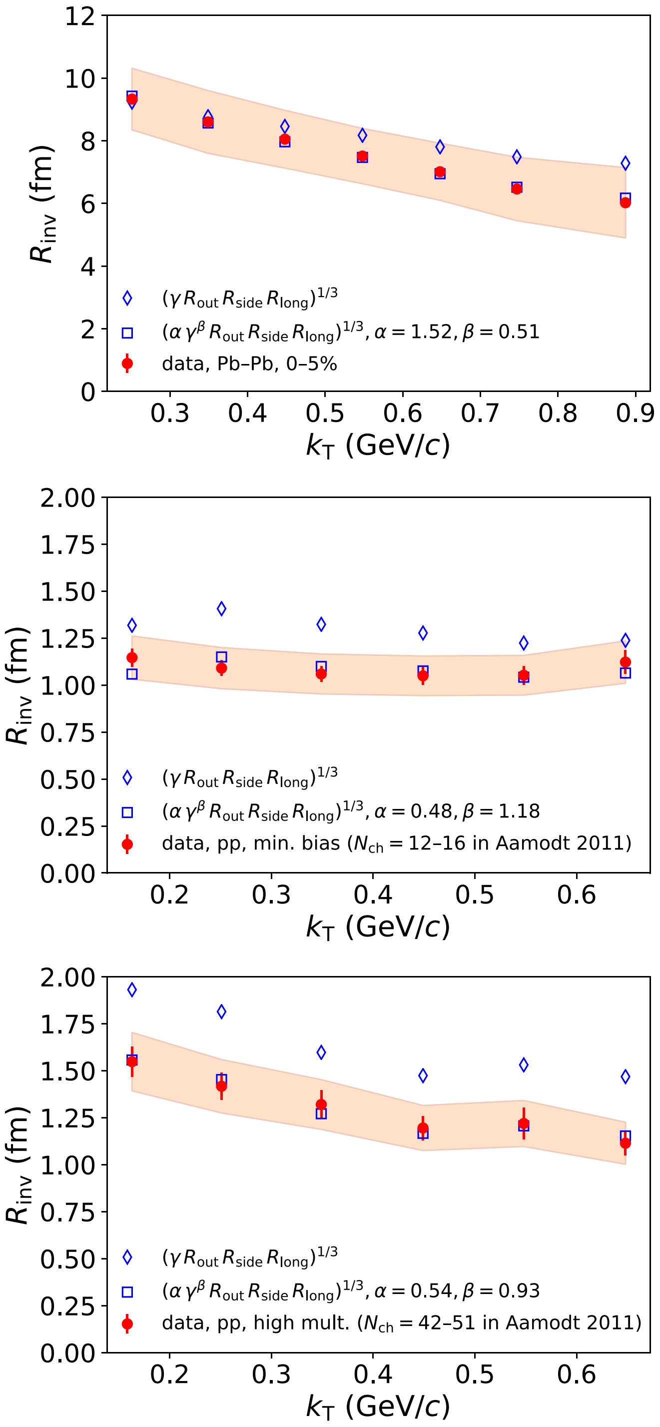

FIG. 9. Comparison of measured one-dimensional HBT radii R_{inv} as a function of the transverse pair momentum k_{T} from the ALICE collaboration and R_{inv} values calculated from measured three-dimensional HBT radii R_{out}, R_{side}, R_{long} according to $R_{\mathrm{inv}}^3 \approx \alpha \gamma^{\beta} R_{\mathrm{out}} R_{\mathrm{side}} R_{\mathrm{long}}$. The bands reflect the uncertainties of the measured R_{inv} values. The calculated R_{inv} values are shown for $\alpha = \beta = 1$ and for the values of α and β which fit the measured R_{inv} radii best. Results are shown for Pb-Pb collisions (centrality 0%–5%) at $\sqrt{s_{\mathrm{NN}}} = 2.76\,\mathrm{TeV}$ [21] (upper panel), "minimum bias" *pp* collisions ($N_{\mathrm{ch}} = 12$–16 in Aamodt [22]) at $\sqrt{s} = 7\,\mathrm{TeV}$ [22] (middle panel), and high-multiplicity *pp* collisions ($N_{\mathrm{ch}} = 42$–51 in Aamodt [22]) at $\sqrt{s} = 7\,\mathrm{TeV}$ [22] (lower panel).

is given by

$$\mathcal{F} = \frac{h(\gamma)}{m_{\rm T}}\frac{(2\pi)^{3/2}}{2J+1}\frac{1}{R_{\rm inv}^3}E\frac{d^3N}{d^3p}. \tag{A2}$$

In this section we use assume $h(\gamma)=\alpha\gamma^{\beta}$ and use data from ALICE [21,22] to determine the values of α and β which best describe the relation between the measured one-dimensional radii $R_{\rm inv}$ and the three-dimensional radii $R_{\rm out}$, $R_{\rm side}$, $R_{\rm long}$. The results are shown in Fig. 9. The best fit values for α and β turn out to be significantly different between Pb-Pb and *pp* collisions. We then use these values to calculate maximum phase space densities according to Eq. (A2). The corresponding results for the entropy and the entropy per final-state charged particle are as follows.

System	dS/dy	$(dS/dy)/(dN_{\rm ch}/dy)$
Pb-Pb, 0%–10%	11534 ± 1188	6.9 ± 0.8
pp minimum bias	41.7 ± 4.1	5.7 ± 0.6
pp high multiplicity	159.0 ± 19.8	6.3 ± 0.8

We note that for Pb-Pb collisions the entropy estimates increases only very slightly. For *pp* collisions, the values for the entropy are higher than our standard results obtain using $\alpha=\beta=1$, but they agree at the 1σ level.

APPENDIX B: TWO-COMPONENT GLAUBER MODEL

In this section we recap the details of the two-component Glauber model used to generate initial conditions for KøMPøST evolution. The nuclear charge density distribution of lead nuclei is parametrized by Wood-Saxon distribution [61],

$$\rho(\vec{r}) = \rho_0\frac{1}{1+\exp\left(\frac{|\vec{r}|-R}{a}\right)}, \tag{B1}$$

where for our purposes we will choose ρ_0 such that the total volume integral of ρ is equal to the number of nucleons $N_A = 208$. Then $\rho_0 = 0.160391\,{\rm fm}^{-3}$, $R = 6.62\,{\rm fm}$, and $a = 0.546\,{\rm fm}$. For Lorentz contracted nuclei, the longitudinal direction can be integrated out to obtain the density per unit transverse area,

$$T(\vec{r}_\perp) = \int_{-\infty}^{\infty}\rho(\vec{r}_\perp, z)dz. \tag{B2}$$

Then the collision probability of two nuclei with N_A and N_B nucleons is given by

$$\frac{dN^{\rm coll}(\vec{r},\vec{b})}{d^2\vec{r}} = T_A(\vec{r})T_B(\vec{r}-\vec{b})\sigma_{\rm inel}^{NN}, \tag{B3}$$

where the radius is implicitly assumed to be in the transverse plane and $\sigma_{\rm inel}^{NN} = 6.4\,{\rm fm}^2$ is the inelastic nucleon-nucleon cross section. The number of participant nucleons per transverse area is given by

$$\begin{aligned}\frac{dN^{\rm part}(\vec{r},\vec{b})}{d^2\vec{r}} &= T_A(\vec{r})\big[1-\big(1-T_B(\vec{r}-\vec{b})\sigma_{\rm inel}^{NN}/N_B\big)^{N_B}\big]\\ &\quad + T_B(\vec{r}-\vec{b})\big[1-\big(1-T_A(\vec{r})\sigma_{\rm inel}^{NN}/N_A\big)^{N_A}\big].\end{aligned} \tag{B4}$$

These probabilities are combined in the two-component Glauber model [56,61] where α is an adjustable parameter,

$$(s\tau)_0 = \kappa_s\left(\frac{1-\alpha}{2}\frac{dN^{\rm part}(\vec{r},\vec{b})}{d^2r} + \alpha\frac{dN^{\rm coll}(\vec{r},\vec{b})}{d^2r}\right). \tag{B5}$$

We use $\alpha = 0.128$, which is the same value as in ALICE publication [56], but with different parametrization of Eq. (B5), namely $\alpha = \frac{1-f}{1+f}$.

---

[1] W. Busza, K. Rajagopal, and W. van der Schee, Ann. Rev. Nucl. Part. Sci. **68**, 339 (2018).

[2] R. Derradi de Souza, T. Koide, and T. Kodama, Prog. Part. Nucl. Phys. **86**, 35 (2016).

[3] B. Müller and A. Schäfer, Int. J. Mod. Phys. E **20**, 2235 (2011).

[4] S. Pal and S. Pratt, Phys. Lett. B **578**, 310 (2004).

[5] J. Sollfrank and U. W. Heinz, Phys. Lett. B **289**, 132 (1992).

[6] B. Muller and K. Rajagopal, Eur. Phys. J. C **43**, 15 (2005).

[7] S. S. Gubser, S. S. Pufu, and A. Yarom, Phys. Rev. D **78**, 066014 (2008).

[8] C. Nonaka, B. Muller, S. A. Bass, and M. Asakawa, Phys. Rev. C **71**, 051901(R) (2005).

[9] J. Berges, K. Reygers, N. Tanji, and R. Venugopalan, Phys. Rev. C **95**, 054904 (2017).

[10] B. Abelev *et al.* (ALICE Collaboration), Phys. Rev. C **88**, 044910 (2013).

[11] B. B. Abelev *et al.* (ALICE Collaboration), Phys. Rev. Lett. **111**, 222301 (2013).

[12] B. B. Abelev *et al.* (ALICE Collaboration), Phys. Lett. B **728**, 216 (2014); **734**, 409(E) (2014).

[13] J. Adam *et al.* (ALICE Collaboration), Eur. Phys. J. C **75**, 226 (2015).

[14] B. Abelev *et al.* (ALICE Collaboration), Phys. Lett. B **712**, 309 (2012).

[15] S. Acharya *et al.* (ALICE Collaboration), Phys. Rev. C **99**, 024906 (2019).

[16] J. Adam *et al.* (ALICE Collaboration), Nature Phys. **13**, 535 (2017).

[17] A. Andronic, P. Braun-Munzinger, K. Redlich, and J. Stachel, Nature (London) **561**, 321 (2018).

[18] G. F. Bertsch, Phys. Rev. Lett. **72**, 2349 (1994); **77**, 789(E) (1996).

[19] D. Ferenc, U. W. Heinz, B. Tomasik, U. A. Wiedemann, and J. G. Cramer, Phys. Lett. B **457**, 347 (1999).

[20] M. A. Lisa, S. Pratt, R. Soltz, and U. Wiedemann, Ann. Rev. Nucl. Part. Sci. **55**, 357 (2005).

[21] J. Adam *et al.* (ALICE Collaboration), Phys. Rev. C **93**, 024905 (2016).

[22] K. Aamodt *et al.* (ALICE Collaboration), Phys. Rev. D **84**, 112004 (2011).

[23] J. Adam *et al.* (ALICE Collaboration), Phys. Rev. C **92**, 054908 (2015).

[24] C. Tsallis, J. Statist. Phys. **52**, 479 (1988).

[25] T. Bhattacharyya, J. Cleymans, L. Marques, S. Mogliacci, and M. W. Paradza, J. Phys. G **45**, 055001 (2018).

[26] A. Kisiel, M. Gałażyn, and P. Bożek, Phys. Rev. C **90**, 064914 (2014).

[27] T. Sjostrand, S. Mrenna, and P. Z. Skands, J. High Energy Phys. 05 (2006) 026.

[28] T. Sjostrand, S. Mrenna, and P. Z. Skands, Comput. Phys. Commun. **178**, 852 (2008).

[29] P. Braun-Munzinger, K. Redlich, and J. Stachel, in *Quark-Gluon Plasma 3*, edited by R. C. Hwa, and X. N. Wang (World Scientific, Singapore, 2004), pp. 491-599.

[30] J. Letessier and J. Rafelski, *Hadrons and Quark-Gluon Plasma* (Cambridge University Press, Cambridge, 2002), Vol. 18.

[31] K. Aamodt *et al.* (ALICE Collaboration), Phys. Rev. Lett. **106**, 032301 (2011).

[32] B. Alver *et al.* (PHOBOS Collaboration), Phys. Rev. C **83**, 024913 (2011).

[33] P. Bożek, Nucl. Phys. A **956**, 208 (2016).

[34] R. D. Weller and P. Romatschke, Phys. Lett. B **774**, 351 (2017).

[35] C. Aidala *et al.* (PHENIX Collaboration), Nat. Phys. **15**, 214 (2019).

[36] J. Berges, S. Floerchinger, and R. Venugopalan, Phys. Lett. B **778**, 442 (2018).

[37] O. K. Baker and D. E. Kharzeev, Phys. Rev. D **98**, 054007 (2018).

[38] J. Adam *et al.* (ALICE Collaboration), Eur. Phys. J. C **77**, 33 (2017).

[39] V. Vovchenko and H. Stoecker, Comput. Phys. Commun. **244**, 295 (2019).

[40] M. Tanabashi *et al.* (Particle Data Group), Phys. Rev. D **98**, 030001 (2018).

[41] P. Braun-Munzinger and J. Stachel, J. Phys. G **28**, 1971 (2002).

[42] A. Andronic, P. Braun-Munzinger, and J. Stachel, Phys. Lett. B **673**, 142 (2009); **678**, 516(E) (2009).

[43] G. Torrieri, S. Steinke, W. Broniowski, W. Florkowski, J. Letessier, and J. Rafelski, Comput. Phys. Commun. **167**, 229 (2005).

[44] G. Torrieri, S. Jeon, J. Letessier, and J. Rafelski, Comput. Phys. Commun. **175**, 635 (2006).

[45] M. Petran, J. Letessier, J. Rafelski, and G. Torrieri, Comput. Phys. Commun. **185**, 2056 (2014).

[46] S. Wheaton and J. Cleymans, Comput. Phys. Commun. **180**, 84 (2009).

[47] A. Kisiel, T. Taluc, W. Broniowski, and W. Florkowski, Comput. Phys. Commun. **174**, 669 (2006).

[48] M. Chojnacki, A. Kisiel, W. Florkowski, and W. Broniowski, Comput. Phys. Commun. **183**, 746 (2012).

[49] A. Andronic, P. Braun-Munzinger, J. Stachel, and M. Winn, Phys. Lett. B **718**, 80 (2012).

[50] J. D. Bjorken, Phys. Rev. D **27**, 140 (1983).

[51] M. Gyulassy and T. Matsui, Phys. Rev. D **29**, 419 (1984).

[52] P. Danielewicz and M. Gyulassy, Phys. Rev. D **31**, 53 (1985).

[53] R. C. Hwa and K. Kajantie, Phys. Rev. D **32**, 1109 (1985).

[54] G. Giacalone, A. Mazeliauskas, and S. Schlichting, arXiv:1908.2866.

[55] H. De Vries, C. W. De Jager, and C. De Vries, Atom. Data Nucl. Data Tabl. **36**, 495 (1987).

[56] B. Abelev *et al.* (ALICE Collaboration), Phys. Rev. C **88**, 044909 (2013).

[57] A. Bazavov *et al.* (HotQCD Collaboration), Phys. Rev. D **90**, 094503 (2014).

[58] S. Borsanyi *et al.*, Nature (London) **539**, 69 (2016).

[59] S. Chatrchyan *et al.* (CMS Collaboration), Phys. Rev. Lett. **109**, 152303 (2012).

[60] J. Adam *et al.* (ALICE Collaboration), Phys. Rev. C **94**, 034903 (2016).

[61] M. L. Miller, K. Reygers, S. J. Sanders, and P. Steinberg, Ann. Rev. Nucl. Part. Sci. **57**, 205 (2007).

[62] A. Kurkela, A. Mazeliauskas, J.-F. Paquet, S. Schlichting, and D. Teaney, Phys. Rev. Lett. **122**, 122302 (2019).

[63] A. Kurkela, A. Mazeliauskas, J.-F. Paquet, S. Schlichting, and D. Teaney, Phys. Rev. C **99**, 034910 (2019).

[64] S. Floerchinger, E. Grossi, and J. Lion, Phys. Rev. C **100**, 014905 (2019).

[65] A. Kurkela and A. Mazeliauskas, Phys. Rev. D **99**, 054018 (2019).

[66] A. Kurkela and A. Mazeliauskas, Phys. Rev. Lett. **122**, 142301 (2019).

[67] J. S. Moreland, J. E. Bernhard, and S. A. Bass, Phys. Rev. C **92**, 011901(R) (2015).

[68] H. Niemi and G. S. Denicol, arXiv:1404.7327.

[69] U. W. Heinz and J. S. Moreland, J. Phys. Conf. Ser. **1271**, 012018 (2019).

[70] A. Kurkela, A. Mazeliauskas, J.-F. Paquet, S. Schlichting, and D. Teaney, KøMPøST: Linearized Kinetic Theory Propagator of Initial Conditions for Heavy Ion Collisions, 2018, https://github.com/KMPST/KoMPoST.